International Communications in Heat and Mass Transfer 136 (2022) 106166

Contents lists available at ScienceDirect

International Communications in Heat and Mass Transfer

journal homepage: www.elsevier.com/locate/ichmt

Surface wettability effects on evaporating meniscus in nanochannels

Mustafa Ozsipahi [a], Yigit Akkus [b,c], Ali Beskok [a,*]

[a] Southern Methodist University, Dallas, TX 75205, USA
[b] Ericsson AB, 164 40 Kista, Sweden
[c] ASELSAN Inc., Ankara 06200, Turkey

ARTICLE INFO

Keywords:
Molecular dynamics
Thin-film evaporation
Phase-change
Wettability
Adsorbed layer

ABSTRACT

Systematic investigations of self-regulation of evaporating menisci in nanochannels are conducted as a function of the surface wettability under various applied heat flux conditions. The simulation system is designed to result in steady-state response so that a stable meniscus region can be produced. Non-equilibrium molecular dynamics simulations are performed for argon fluid in platinum channels. Depending on the surface wettability and the applied heat flux the meniscus can be in the pinned regime or it can recede inside the channel. Adsorbed layer formation becomes evident for the latter case. Higher wettability enables the formation of a thicker adsorbed layer reducing the radius of curvature of the meniscus and the overall evaporation rate in the channel. Adsorbed layer reduces the thermal resistance of the evaporator, providing a higher critical heat flux. While evaporation from the adsorbed layer is negligible for macroscopic systems, it can contribute up to 80% of the total evaporating mass in nanoscale systems. The current work provides insights into the capillary-driven thin-film evaporation in ultra-small channels and the findings are meaningful for next-generation thermal management systems.

1. Introduction

Heat fluxes experienced in high-performance integrated circuits, power electronics, and laser diodes can reach several hundreds of Watts per square centimeter [1,2]. Several thermal management techniques such as immersion cooling, embedded cooling, and jet impingement of coolant on chip surfaces have been proposed to address these challenges. Although convective cooling can dissipate heat fluxes as high as 1 kW/cm^2, it requires large pumping power that results in a low coefficient of performance [3,4]. Two-phase flow cooling techniques utilizing the latent heat of evaporation can provide a desirable solution for high heat flux demands [5].

Among the two-phase cooling techniques, thin-film evaporation is considered one of the most promising approaches because of its' stable, bubble-free nature. However, this process requires continuous liquid supply to the thin-film region, which can be established by passive capillary pumping techniques [6,7]. Optimal pumping performance requires minimizing the viscous effects while maximizing the Laplace pressure which is a function of the surface tension and the radius of curvature (ROC) of the capillary. Reducing the capillary size can be beneficial due to the onset of liquid slip that decreases the viscous drag [8], and also controls the ROC. With the onset of micro- and nano-fabrication techniques, several researchers have investigated thin-film evaporation from nanoporous membranes and nanostructured surfaces.

Wang and her coauthors have investigated evaporation from nanoporous aluminum membranes and reported heat fluxes above 500 W/cm^2 across the interface over a total evaporation area of 0.20 mm^2 [9]. Different heat transfer regimes are demonstrated and more than an order of magnitude change in the dissipated heat flux is observed depending on the evaporation regime [10]. Nanoporous silicon membrane with a ~100 nm diameter is fabricated and heat fluxes of 665 ± 74 W/cm^2 is reported using pentane, which has low surface tension [11]. Other liquids like R245fa showed nearly 10 folds enhancement in heat dissipation when *compared* with that of water under the same working conditions [12]. Since the meniscus dynamics in nanoscale confinements is highly affected by the solid-fluid interactions, effects of surface wettability on evaporation was also investigated. Liquid flooding over the nanopores was prevented by rendering these surfaces hydrophobic [13]; and the effects of hydrophilic/hydrophobic evaporator surfaces were investigated using a hybrid nanochannel-nanopore design [14]. Evaporation fluxes that are 11 times larger than the maximum theoretical value obtained by the Hertz-Knudsen model were reported

* Corresponding author.
E-mail address: abeskok@smu.edu (A. Beskok).

https://doi.org/10.1016/j.icheatmasstransfer.2022.106166

for hydrophilic evaporator surfaces [14].

Antao et al. measured the dynamic behavior of the evaporating liquid-vapor interface in micropillar arrays using a transient laser interferometry technique and reported pinned and receding meniscus regimes during the dynamic evaporation process [15]. The maximum capillary pressure was reported in the receding regime, which was determined by the receding contact angle [15]. Visualization of the evaporating liquid-vapor interface revealed that the receding regime occurred when the capillary pressure generated at a measured meniscus ROC curvature could not balance the viscous loss resulting from flow through the micropillar array [16]. The shape of the receding meniscus was independent of the applied heat, and only depended on the micropillar array geometry and the intrinsic wettability of the material. Theoretical investigation of the self-regulation of the shape and position of the meniscus in response to different operating conditions showed that evaporation from the nanopores was not a locally expressible phenomenon. The shape and position of the meniscus affected the overall heat and mass flux, and therefore, the interfacial mass flux could not be calculated simply using the local pressure and temperature [17]. These results showed the prominence of transient meniscus dynamics on thin-film evaporation.

Several researchers conducted molecular dynamics (MD) simulations of thin-film evaporation processes [18–21]. However, most of these studies utilized a flat liquid thin-film region heated from the bottom while a surface on the top was cooled at the same rate. These computational studies totally ignored the capillary pumping that feeds the thin-film. As a result, they either observed transient evaporation of the thin-film, or they maintained a steady evaporation process by removing the evaporating molecules. While the former approach is difficult to characterize due to its transient nature, the latter approach produces a vapor concentration gradient that results in lyophilic surfaces with higher evaporation fluxes than expected. Overall, deleting the evaporating atoms results in higher mass flow rates than expected.

Proper investigations of thin-film evaporation should include the capillary pumping that feeds the evaporation process and at the same time, be able to create steady transport with stable liquid-vapor interfaces in the evaporator/condenser sections of the domain. In [22], we investigated evaporation and condensation from a liquid argon sandwiched between two parallel plates by adding and removing equal amounts of heat from the evaporator and condenser regions of the channel, respectively. This computational system allows self-regulation of the vapor-liquid interface with respect to different operating conditions by continuously pumping liquid to the thin-film region. The vapor molecules move towards the condenser region and eventually condense to maintain a steady operation. An important finding in [23] was the discovery of evaporation from the adsorbed layer, which was not reported before. This new phenomenon can shed light on the reasons for the high evaporation rates reported in recent experiments [11,14]. In a proceeding study, we introduced an energy-based interface detection method that eliminates the need to use an arbitrary density cut-off value to determine the liquid-vapor interface [24]. This new method results in smooth liquid-vapor interfaces that are not affected by the typical density fluctuations near the surfaces, and it properly models the thin-film regions near the solid-liquid-vapor trijunction [24].

The *objective* of the current study is to investigate the surface wettability effects on the evaporating meniscus under different heating/cooling (H/C) conditions. For simplicity, we use argon fluid and platinum walls and consider van der Waals interactions between the fluid-fluid and fluid-surface atoms. Using such a simplistic computational approach, we present the dynamics of thin-film evaporation and observed self-regulation of the meniscus region and formation of the adsorbed layer as a function of the surface wettability and applied heat fluxes. Thermal performance of the evaporator is also investigated and thermal resistance and maximum critical heat flux are presented.

2. MD simulation details

We simulated phase-change driven argon flow between two parallel platinum plates separated with a 3.92 nm distance using three-dimensional MD simulations. Dimensions of the simulation domain are set as 31.360 × 5.096 × 3.724 nm in the lateral (*x*-), vertical (*y*-), and longitudinal directions (*z*-), respectively. Perspective and the side view of the MD simulation domain with its physical dimensions are shown in Fig. 1. LAMMPS (Large-scale Atomic/Molecular Massively Parallel Simulator) is used as the MD solver [25]. Periodic boundary conditions are employed in three directions. The thickness of the solid walls is 0.588 nm. The nanochannel consists of 4 layers of Pt molecules and has a face-centered cubic structure (FCC) using a lattice constant of 3.92 Å. The (1,0,0) plane of the wall is facing the fluid, and the outermost wall atoms are fixed in their original lattice location, resulting in a constant simulation domain volume. Embedded-atom method is employed for the interatomic forces of Pt atoms [26].

Interactions between the fluid-fluid and fluid-wall molecules are modeled using the truncated Lennard-Jones (LJ) 12–6 potential given by

$$V_{trnc}(r_{ij}) = 4\varepsilon\left[\left(\left(\frac{\sigma}{r_{ij}}\right)^{12} - \left(\frac{\sigma}{r_{ij}}\right)^{6}\right) - \left(\left(\frac{\sigma}{r_c}\right)^{12} - \left(\frac{\sigma}{r_c}\right)^{6}\right)\right]$$

where ε is the depth of the potential well, σ is the molecular diameter, r is the molecular distance. We utilized σ_{Ar}=0.34 nm, σ_{Pt}=0.27 nm, σ_{Ar-Pt}=0.3085 nm, and ε_{Ar}=0.01042 eV [27]. For faster calculations, the LJ interactions utilized a cutoff distance of $r_c = 3\sigma_{Ar}$. The argon-platinum interaction parameter ε_{Ar-Pt}, is directly related to the wettability of the surface [27,28]. Here we selected $\varepsilon_{Ar-Pt} = 0.0055798$ eV and increased this value to $3\varepsilon_{Ar-Pt}$ and $5\varepsilon_{Ar-Pt}$ to investigate the effects of fluid-solid interaction potential on thin film evaporation.

Simulations started with Maxwell-Boltzmann velocity distribution for all atoms at 110 K. The Newton's equation of motion for each atom is integrated with 5 fs time steps using the Verlet algorithm. First canonical ensemble (NVT) is imposed for 10 ns to reach an isothermal state at 110 K by using the Nose-Hoover thermostat. This is followed by applying microcanonical ensemble (NVE) on Ar atoms for another 10 ns, while keeping the Pt atoms at 110 K using the same thermostat. At the end of this second stage, two stable menisci form at the channel tips as shown in Fig. 1c. It is important to indicate that the thermophysical properties of liquid argon in nanoconfinements can be significantly different than that of bulk fluids [8]. The total number of Ar atoms in each wettability case is carefully selected to keep the quality factor constant. Having the same density, temperature and quality factor for Ar fix the initial thermodynamic state for each investigated case. To fix the thermodynamic state for all simulations, the numbers of vapor and liquid atoms were calculated by a posteriori simulation and the total number of argon atoms is precisely reiterated to have the same mixture quality value. In this context, the total number of Ar molecules in the simulation increased with increasing wall-fluid interaction parameters. The number of Ar atoms used in the simulations is 4200, 4885, and 5045 for ε_{Ar-Pt}, $3\varepsilon_{Ar-Pt}$, and $5\varepsilon_{Ar-Pt}$ cases, respectively. The nanochannel consists of 6400 Pt atoms.

In the third stage, nonequilibrium MD (NEMD) simulations are carried out for 30 ns by applying equal energy addition and extraction to the evaporator and condenser zones of the channel, respectively. The added/extracted energy levels varied from 5 nW to 14 nW for each case. In order to avoid axial heat conduction through the walls, Pt molecules in the middle regions of the nanochannel were not allowed to vibrate (i.e., thermally frozen) but allowed to have LJ interactions with the neighboring Ar atoms. The simulation system goes through transients and reaches a steady-state within the initial 10 ns. Last 20 ns of the NEMD simulations are used to obtain 1 million independent samples for time-averaged temperature, density, kinetic energy, potential energy, and velocity distributions in the domain. The data is processed using rectangular prism bins extending Δz = 3.724 nm in the longitudinal

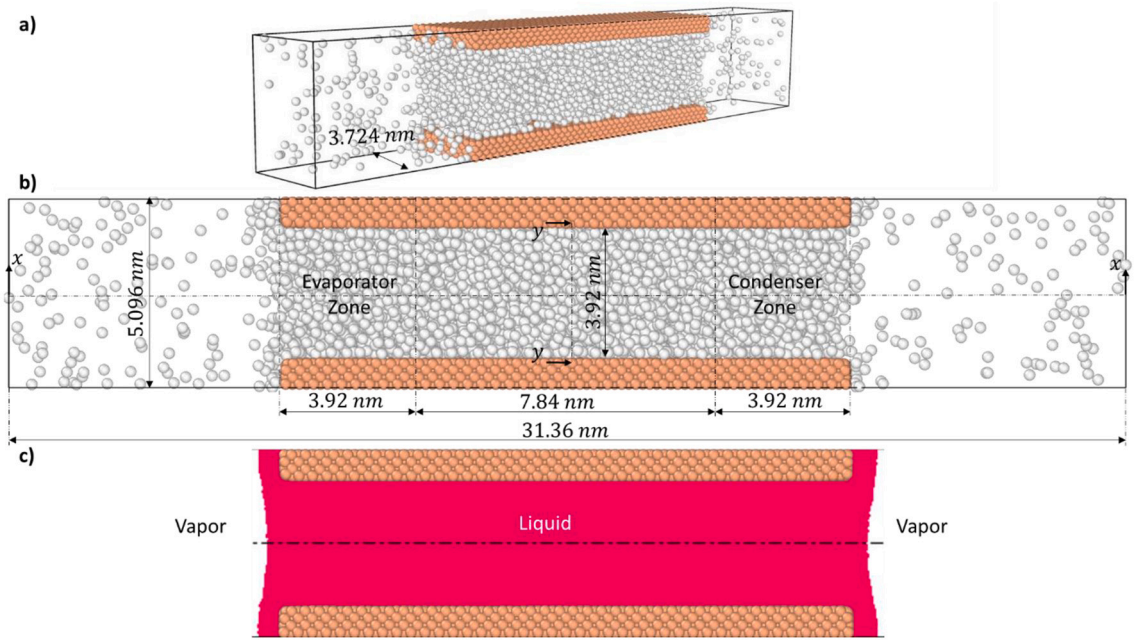

Fig. 1. a) The perspective view and b) side view of the MD simulation domain with pertinent dimensions. The 3D channel geometry extends 3.724 nm in the longitudinal (z-) direction. Argon and platinum molecules are shown with gray and orange spheres, respectively. The figure also shows the evaporator and condenser regions of the domain, where constant heat addition and subtraction are applied, respectively. This creates a 2D steady flow system with evaporating meniscus and condenser regions. c) Formation of two stable menisci during the microcanonical equilibrium simulation.

direction. Wall temperatures such as evaporator and condenser are evaluated using bins with $\Delta x = \sigma_{Pt}$ and $\Delta y = 3\sigma_{Pt}$, while the fluid properties are calculated using rectangular bins with $\Delta x = \frac{\sigma}{7}$ and $\Delta y = \frac{\sigma}{7}$.

A liquid density of 1180 kg/m^3 is maintained at the channel centerline, which drops to 48 kg/m^3 for the vapor phase across an interface region with a typical thickness of ~2 nm. The $3\varepsilon_{Ar-Pt}$ and $5\varepsilon_{Ar-Pt}$ cases result in similar interface locations where the ε_{Ar-Pt} case yields an interface closer to the channel tips. The liquid density profiles obtained at the middle of the channel (y-y axis in Fig. 1) is presented in Fig. 2b. Density fluctuations within $3\sigma_{Ar}$ distance from the walls increase in magnitude with increased ε_{Ar-Pt} values. The channel height used in this study is large enough to obtain a constant density region at the channel center for each wetting case.

The exact location of the liquid/vapor interface has paramount importance in evaporation studies. Most previous researchers used arbitrary density-cutoff values to determine the interface location. However, this approach suffers from density oscillations near the walls. In [24], we defined the liquid-vapor interface for monatomic fluids at a location where the kinetic energy (KE) of the fluid molecules first exceeded the magnitude of the total potential energy (PE) exerted on them by their neighboring atoms. This concept is implemented using bin-based calculations, where KE is a function of the local temperature, and the magnitude of the PE depends on the local density and the LJ interaction parameters. For fluid atoms near the solid boundaries, PE imposed on the fluid molecules by the walls is also included in calculations.

3. Results and discussion

Overall, 24 NEMD simulations are carried out to investigate the

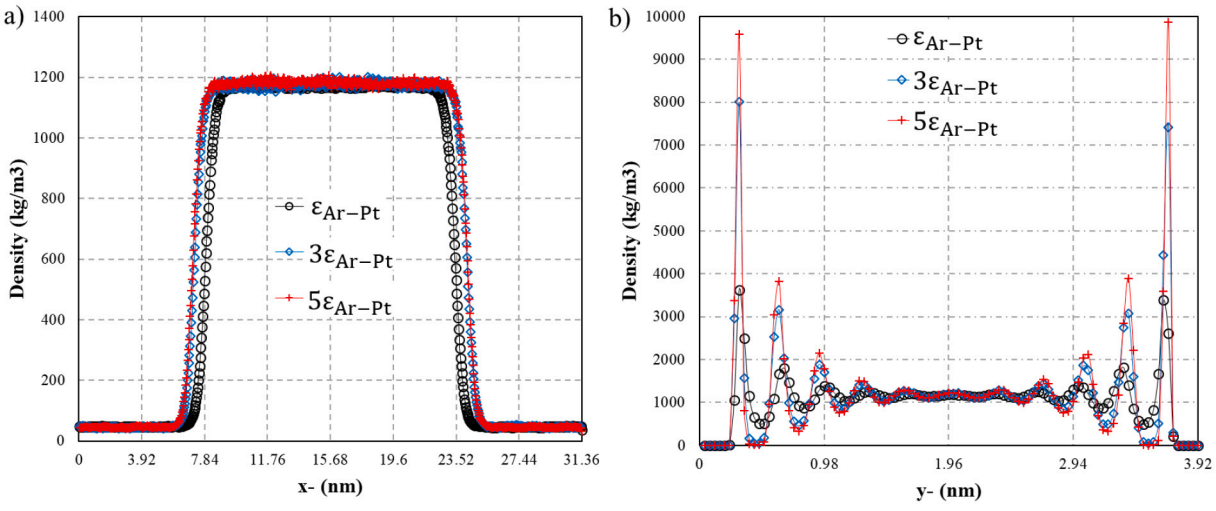

Fig. 2. Density distributions along the a) x-x and b) y-y axis for different wall fluid interaction potentials during the microcanonical (NVE) ensemble stage. Figure a) and b) uses a ribbon cut with ~3.5 σ_{Pt} thickness in x- and y- direction.

evaporating meniscus in nanochannels. A schematic description of self-regulation of evaporating meniscus for wetting cases is shown in Fig. 3. When the interfacial pressure difference is relatively small, the meniscus is pinned (Region I) to the tip of the nanochannel. This is also called as the pinned regime in experimental studies [15,16]. Upon increasing the energy input rate, the radius of curvature (ROC) in the evaporator zone starts to decrease, and the meniscus shifts from the pinned region to the receding regime (Region II) in order to compensate for the pressure drop inside the nanochannel [15]. ROC stays nearly the same in the receding regime, whereas the meniscus adjusts its axial position and recedes further into the channel upon increasing the energy rate. Region III indicates the superheated absorbed layer regime where the evaporating meniscus passes the heating zone. Therefore, heat transfer in this regime occurs between the heated Pt walls and the adsorbed layer. This evaporating meniscus description is mostly valid for highly wetting cases, in which, the adsorbed layer formation is evident under the receding regime. For low wall-fluid interaction potentials, the adsorbed layer may not form at all, and the system may quickly switch from the pinned regime to complete dry-out once the heating rate is increased beyond a certain level.

Fig. 4 presents comparisons of evaporating meniscus profiles for three different wetting cases obtained at three different heating/cooling (H/C) rates. The first, second and third rows in the figure present the evaporating meniscus profiles for the ε_{Ar-Pt}, $3\varepsilon_{Ar-Pt}$, and $5\varepsilon_{Ar-Pt}$ cases, respectively. The effect of H/C is presented while applying 5 nW, 8 nW and 10 nW for each case. The evaporating meniscus profiles are in the pinned region for all wetting cases at 5 nW H/C. Increasing the H/C to 8 nW, the higher wettability cases ($3\varepsilon_{Ar-Pt}$, and $5\varepsilon_{Ar-Pt}$) present different evaporating meniscus regimes than the ε_{Ar-Pt} case, where the evaporating meniscus shifts from pinned to the receding regime, displaying adsorbed layer formation. Further increasing the H/C to 10 nW, the meniscus recedes more into the channel and adsorbed layer elongates as shown in the right panel. The $5\varepsilon_{Ar-Pt}$ cases produce a thicker adsorbed layer, which prolongs the transition from pinned to the receding regime compared to the $3\varepsilon_{Ar-Pt}$ case. Whereas the ε_{Ar-Pt} case has weaker potential energy near the wall and adsorbed layer is not formed in the simulations as seen in the top row of the figure. Column-based comparison of the receding meniscus position in Fig. 4 show non-monotonic relationship of wall-fluid interaction strength. In order to investigate this, the kinetic and potential energies of the evaporator section and y-y plane (channel middle) are investigated next.

Fig. 5a presents the kinetic and potential energy distributions inside the evaporator region shown with a gray box in the right panel of Fig. 4. Since the kinetic energy is a function of the local temperature of argon molecules, the kinetic energy values are nearly constant and has a positive value. On the other hand, energy-well induced by the LJ interactions lead to attractive (negative) potential energy. Higher wall-fluid interaction strength creates higher potential energy near the wall resulting in a thicker adsorbed layer, and therefore, smaller ROC as shown in Fig. 4. The potential energy profiles obtained in the *y-y* axis (at channel middle) are shown in Fig. 5b. Unlike the $3\varepsilon_{Ar-Pt}$ and $5\varepsilon_{Ar-Pt}$ cases, the ε_{Ar-Pt} case does not exhibit a potential energy peak near the wall. The potential energy peaks near the walls are larger inside the channel than the evaporator regions, since the fluid molecules in the channel are surrounded by walls and high-density liquid molecules. However, fluid molecules in the evaporator region neighbors the walls, and Ar molecules in the adsorbed layer and vapor regions of the domain. Based on our definition of the interface at the location where the KE of molecules first exceeded the magnitude of the local PE, the exact locations of the interface for different wetting cases in Fig. 4 right panel can be associated with the results shown in Fig. 5a. In the middle of the channel, the local KE of Ar molecules are always smaller than the local PE magnitude. Therefore, the local KE distribution is not shown in Fig. 5b.

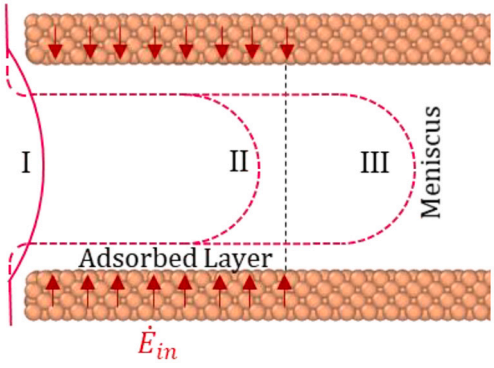

Fig. 3. Schematics of the pinned (I), receding (II) and superheated adsorbed layer (III) evaporating meniscus profiles in nanoconfinements. Red arrows indicate the evaporator zone. Initially, the meniscus is pinned at the tip of the nanochannel. Increasing the energy rate, the meniscus starts to recede into the channel (II) revealing the adsorbed layer. In this region, heat is transferred from walls to both adsorbed layer and meniscus, whereas in the superheated adsorbed layer region (III) heat transfers mainly onto the adsorbed layer. (For interpretation of the references to colour in this figure legend, the reader is referred to the web version of this article.)

Fig. 6 shows the evaporating meniscus profiles for $5\varepsilon_{Ar-Pt}$ case at different H/C rates. The interfaces in the condenser region remain flat, and are not shown in the figures. Initially, the meniscus is pinned to the channel tip at 5 nW. With increasing the supplied energy rate, the liquid-vapor interface moves into the channel (receding regime II), revealing the adsorbed layer. The adsorbed layer has a thickness of nearly $3\sigma_{Ar}$ at this fluid-wall interaction potential. For the 7, 9 and 10 nW cases the meniscus is within the evaporator region of the simulation domain. Therefore, the added energy heats both the meniscus and adsorbed layer regions of the fluid at these H/C rates. As stated earlier in Section 2, walls in the middle section of the channel are thermally frozen so that axial conduction through the Pt walls is eliminated. This was done on purpose to ensure that all added heat would transfer through Ar and eventually be removed by the condenser region on the walls. Otherwise, the axial conduction through the channel would be the most dominant heat transfer mechanism in the simulations. For H/C rates larger than 10 nW the meniscus region moves towards the channel middle, resulting in heat transfer between the Pt walls and thin adsorbed layer (region III in Fig. 3). The thickness of the adsorbed layer continuously decreases with the increased energy rate. MD simulations after 14 nW failed due to dry-out of nanochannel, where the evaporating meniscus receded nearly to the middle of the channel.

Evaporator temperature (T_{ev}), condenser temperature (T_{con}), vapor temperature (T_v) and the thermal resistance of the evaporator region (R_{th}) are given in Table 1. The thermal resistance of the evaporator region is expressed as;

$$R_{th} = \frac{T_v - T_{ev}}{\dot{E}_{in}}$$

where $\dot{E}_{in}$ is the supplied energy rate. The vapor temperature is calculated using 0.82 nm thick vertical slabs in the vapor region located on the left side of the evaporator region. The averaged thermal resistance values for ε_{Ar-Pt}, $3\varepsilon_{Ar-Pt}$, and $5\varepsilon_{Ar-Pt}$ cases are calculated as 3.47, 1.49, and 1.29 K/nW, respectively. Thermal resistance decreases with increased surface wettability due to better heat transfer between the solid and fluid molecules at the interface. For a given H/C in the system, lower evaporator and higher condenser temperatures are calculated for the $5\varepsilon_{Ar-Pt}$ case. This shows that the higher wall-fluid interaction potential can supply higher superheat temperatures ($T_{ev} - T_s$) that are as high as 93.92 K, delaying the dry-out of the device. On the other hand, the ε_{Ar-Pt} case shows a slower transition from pinned (I) to the receding regime (II). Increasing heating further results in dry-out. Table 1 identifies regimes II and III with light and darker filled boxes, respectively. In

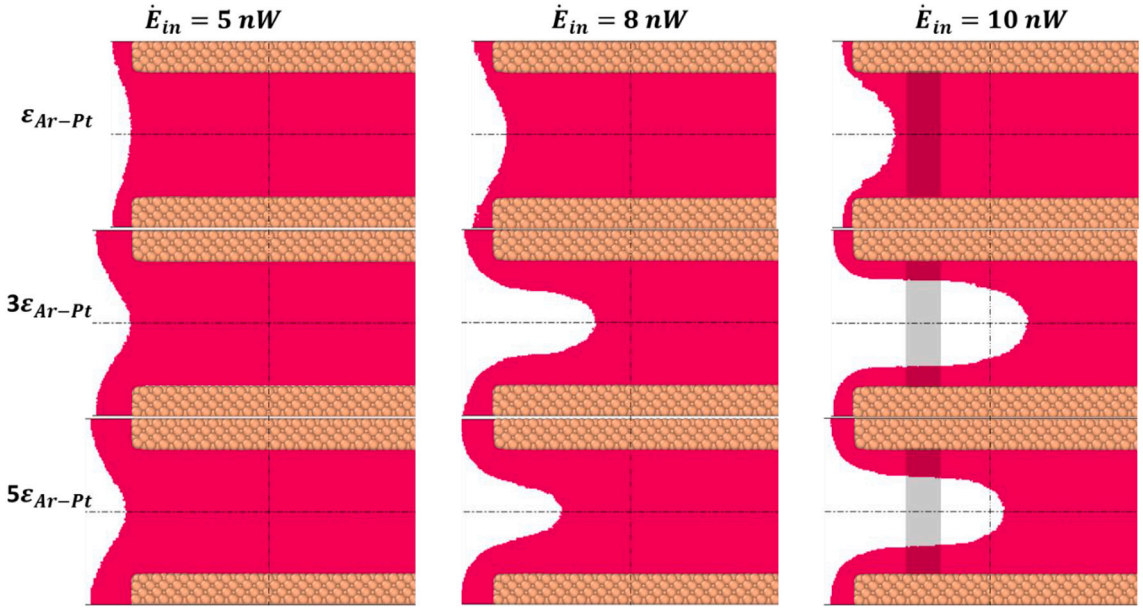

Fig. 4. Evaporating meniscus profiles as a function of the heating rate and wall-fluid interaction potential. The meniscus profiles are pinned for the ε_{Ar-Pt} case and 5 nW heating case (first row and first column, respectively). Increasing the wall-fluid interaction potential increases the adsorbed layer thickness, resulting in a smaller evaporation area and thus smaller ROC. Left sides of the vertical lines show the evaporator zones in the Pt walls.

regime III the evaporator temperature increases faster than the vapor temperature, leading to a higher evaporator thermal resistance for all cases.

Fig. 7a presents the channel mass flow rate for all cases as a function of the supplied energy rate. The channel mass flow rate is calculated using the axial fluid velocity and density at the y-y axis (middle of the channel). Hollow symbols in the figure show the pinned regime, while the solid symbols show regimes II and III. Mass flowrate for the ε_{Ar-Pt} case is larger than the other two cases, and it increases nearly linearly with the supplied energy. However, this system transitions from the pinned regime to regimes II and III very quickly and results in dry-out beyond 11 nW. In the receding regime, the variation of the mass flow rate is slightly affected by the energy addition rate. Capillary pumping decreases in this regime, and the adsorbed layer transport increases. Contrary to the previously published MD studies on thin-film evaporation, higher wettability cases create a thicker adsorbed layer with reduced capillary pumping that results in a lower mass flow rate in the nanochannel. A closer look at the adsorbed layer profiles using $5\varepsilon_{Ar-Pt}$ in Fig. 6b, the ratio of the adsorbed layer thickness to a channel height is 45% and 25% at 10 nW and 14 nW H/C, respectively.

Fig. 7b presents the total and adsorbed layer mass flowrates for the $5\varepsilon_{Ar-Pt}$ case for H/C values in 10 nW to 14 nW range. The adsorbed layer mass flow rate is calculated using the local fluid velocity and density via a control volume analysis, as described in detail in [23]. The evaporating meniscus is in the receding regime and mass flow rate of the channel decreases with increasing the energy rate. When the evaporating meniscus further recedes into the channel, the transmission probability of Ar vapor from the interface to the channel outlet decreases. This leads to a decrease in the capillary transport. Moreover, the contribution of the mass transport through adsorbed layers is increasing with the increased energy rate. The reason for this is the transition between the receding regime (II) to the superheated adsorbed layer regime (III).

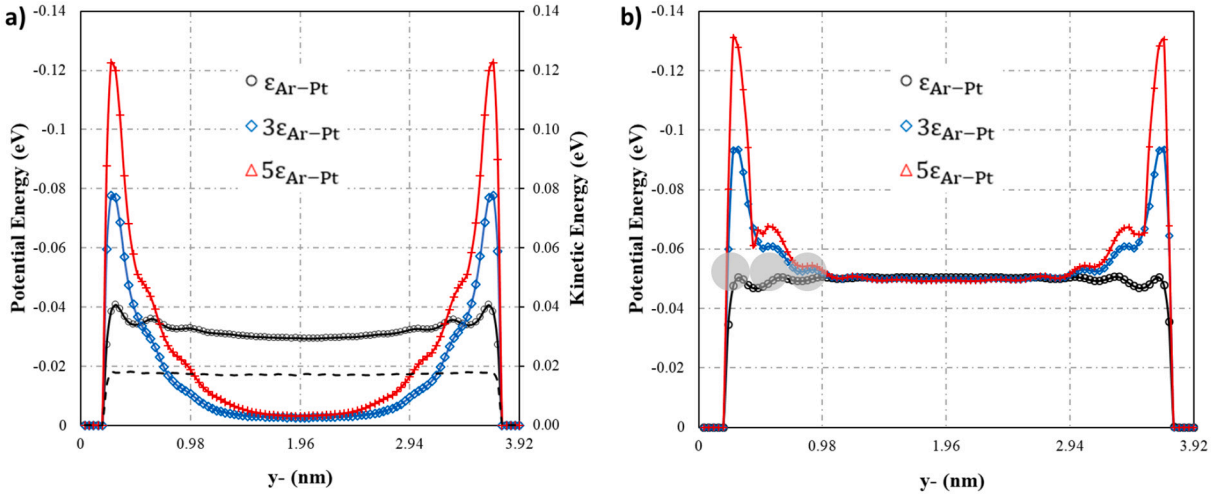

Fig. 5. (a) Kinetic (dashed lines) and potential energy (solid lines) distributions in the evaporator region. (b) Potential energy distributions along *y-y* axis at channel middle. Increasing the wall-fluid interaction potential results in a greater potential field near the wall. The wall effects diminish typically $3\sigma_{Ar}$ away from the wall resulting in flat potential energy profiles at the channel middle. Typical molecular sizes are also shown in the right figure to indicate the scale.

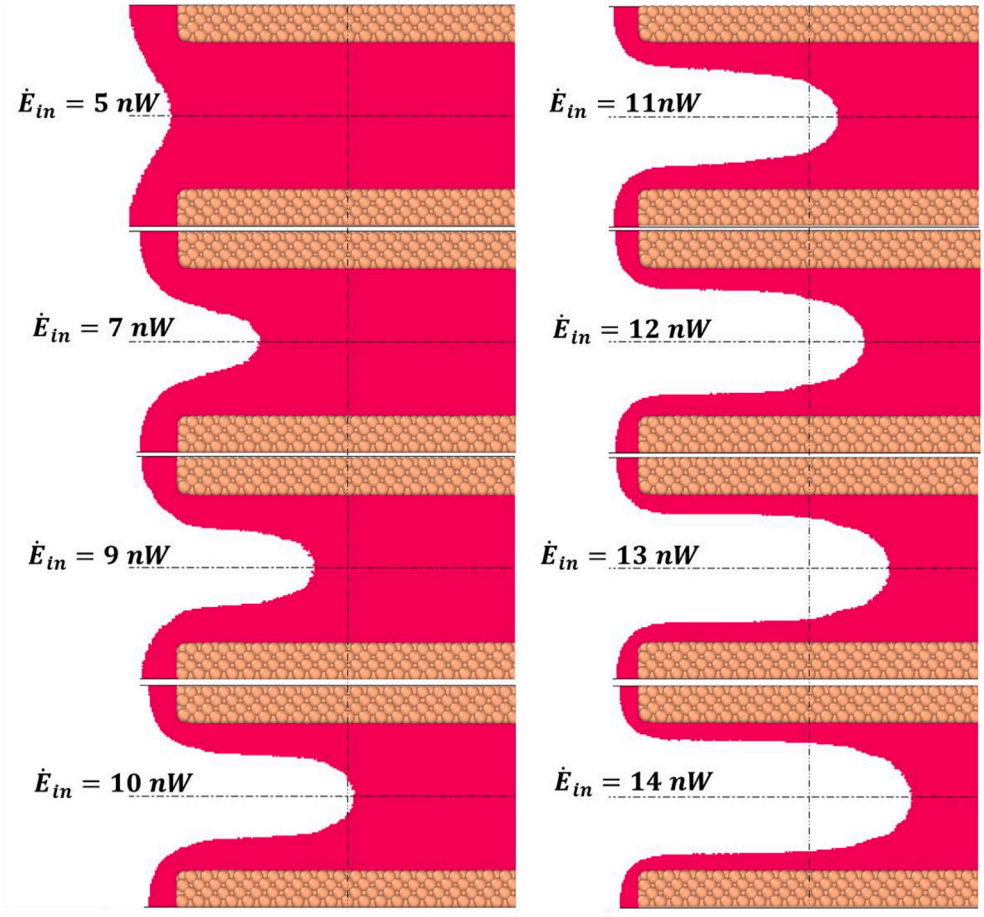

Fig. 6. The liquid-vapor interface at the evaporator section for the $5\varepsilon_{Ar-Pt}$ case at various supplied energy rates. Transition from the pinned to receding to superheated adsorbed layer regimes is presented.

Table 1
The vapor, evaporator and condenser temperatures, and evaporator thermal resistance as a function of the applied H/C rate for the ε_{Ar-Pt}, $3\varepsilon_{Ar-Pt}$ and $5\varepsilon_{Ar-Pt}$ cases. The white, gray and black boxes indicate the interfaces in the pinned (I), receding (II), and superheated adsorbed layer (III) regimes, respectively. Further increasing of H/C beyond region III results in dry-out.

	ε_{Ar-Pt}				$3\varepsilon_{Ar-Pt}$				$5\varepsilon_{Ar-Pt}$			
Ė (nW)	**T_{ev}(K)**	**T_{con}(K)**	**T_v(K)**	**R_{th} (K/nW)**	**T_{ev}(K)**	**T_{con}(K)**	**T_v(K)**	**R_{th} (K/nW)**	**T_{ev}(K)**	**T_{con}(K)**	**T_v(K)**	**R_{th} (K/nW)**
5	127.44	93.25	111.80	3.13	118.82	99.36	110.70	1.62	116.80	99.79	110.50	1.26
6	131.34	90.23	109.20	3.69	120.93	97.25	114.00	1.15	118.91	97.63	114.00	0.82
7	134.87	87.06	113.80	3.01	124.22	95.05	115.80	1.20	121.12	95.97	113.00	1.16
8	138.96	84.21	111.90	3.38	130.65	92.74	118.80	1.48	124.64	93.89	116.30	1.04
9	143.37	81.87	114.10	3.25	137.56	89.91	126.20	1.26	130.85	92.14	123.90	0.77
10	150.23	79.15	116.10	3.41	149.83	86.91	133.10	1.67	138.71	89.29	126.80	1.19
11	176.81	75.34	128.30	4.41	166.14	83.51	143.70	2.04	147.51	86.75	133.50	1.27
12	Dry-Out				Dry-Out				160.70	83.65	143.70	1.42
13									181.11	79.28	156.00	1.93
14									203.92	73.46	174.90	2.07

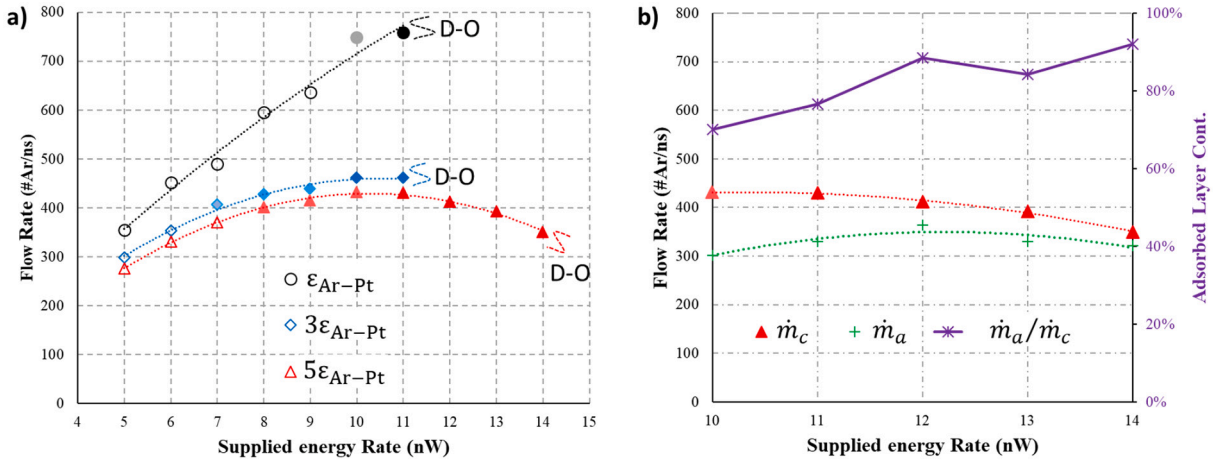

Fig. 7. Channel mass flow rate as a function of the heating rate for various wall fluid interaction potential cases (a). Hollow symbols present the pinned regime of the evaporating meniscus and filled symbols represent regimes II and III. Total and adsorbed layer mass flow rates as a function of the heating rate for the $5\varepsilon_{Ar-Pt}$ case (left ordinate) and the percentile contribution of the absorbed layer transport to the total flowrate (right ordinate) (b). D—O indicate 'dry-out' of the nanochannel.

Primarily in regime III, the meniscus moves closer to the channel middle and more than 80% of the mass transport is due to evaporation from the adsorbed layer, which is a unique aspect of thin-film evaporation from nanochannels.

4. Conclusions

MD simulations are performed to explore self-regulation of the evaporating meniscus under different wall fluid interaction potentials using various heating/cooling (H/C) rates. We found that the evaporating meniscus shape highly depends on the wall-fluid interaction parameter. The adsorbed layer formation becomes evident when the meniscus recedes into the channel, especially for wetting fluids. Adsorbed layer reduces the thermal resistance in the evaporator, providing a higher critical heat flux. Evaporation rate is calculated by evaluating the mass flow rate through the channel. Higher wettability cases create a thicker adsorbed layer followed by reduced capillary pumping and lower mass flow rates. The evaporating meniscus profiles for the $5\varepsilon_{Ar-Pt}$ case are investigated and the transition from pinned to the superheated adsorbed regime is displayed in detail. The channel mass flow rate and mass transport through the adsorbed layer is presented in the superheated adsorbed layer regime. While evaporation from the adsorbed layer is neglected in macroscopic studies, the adsorbed layer transport can contribute up to 80% of the total evaporating mass in nanoscale systems. The results of this study provide significant insights for self-regulation of the shape and position of the evaporating meniscus in response to various operating conditions in nanochannels and emphasize the importance of adsorbed layer transport in ultra-small confinements.

CRediT authorship contribution statement

Mustafa Ozsipahi: Conceptualization, Methodology, Formal analysis, Visualization, Writing – original draft. **Yigit Akkus:** Methodology. **Ali Beskok:** Conceptualization, Supervision, Writing – review & editing.

Declaration of Competing Interest

The authors declare that they have no known competing financial interests or personal relationships that could have appeared to influence the work reported in this paper.

Acknowledgements

This material is based upon work supported by the National Science Foundation under Grant No. CBET 2042239. M.O. acknowledges the financial support by the Turkish Scientific and Technological Research Council under the project 1059B192000153. Computations were carried out using high-performance computing facilities of the Center for Scientific Computation at Southern Methodist University.

References

[1] E. Pop, Energy dissipation and transport in nanoscale devices, Nano Res. 3 (3) (2010) 147–169.
[2] A. Bar-Cohen, J.J. Maurer, J.G. Felbinger, DARPA's intra/interchip enhanced cooling (ICECool) program, in: CS MANTECH Conference, May 13th–16th, 2013.
[3] R. Zhang, M. Hodes, N. Lower, R. Wilcoxon, Water-based microchannel and Galinstan-based minichannel cooling beyond 1 kW/cm^2 $ heat flux, IEEE Trans. Compon. Packag. Manuf. Technol. 5 (6) (2015) 762–770.
[4] A.J. Robinson, R. Kempers, J. Colenbrander, N. Bushnell, R. Chen, A single phase hybrid micro heat sink using impinging micro-jet arrays and microchannels, Appl. Therm. Eng. 136 (2018) 408–418.
[5] G. Vaartstra, L. Zhang, Z. Lu, C.D. Díaz-Marín, J.C. Grossman, E.N. Wang, Capillary-fed, thin film evaporation devices, J. Appl. Phys. 128 (13) (2020), 130901.
[6] M. Nazari, A. Masoudi, P. Jafari, P. Irajizad, V. Kashyap, H. Ghasemi, Ultrahigh evaporative heat fluxes in nanoconfined geometries, Langmuir 35 (1) (2018) 78–85.
[7] Y. Akkus, C.T. Nguyen, A.T. Celebi, A. Beskok, A first look at the performance of nano-grooved heat pipes, Int. J. Heat Mass Transf. 132 (2019) 280–287.
[8] G. Karniadakis, A. Beskok, N. Aluru, Microflows and Nanoflows: Fundamentals and Simulation vol. 29, Springer Science & Business Media, 2005.
[9] Z. Lu, K.L. Wilke, D.J. Preston, I. Kinefuchi, E. Chang-Davidson, E.N. Wang, An ultrathin nanoporous membrane evaporator, Nano Lett. 17 (10) (2017) 6217–6220.
[10] K.L. Wilke, B. Barabadi, Z. Lu, T. Zhang, E.N. Wang, Parametric study of thin film evaporation from nanoporous membranes, Appl. Phys. Lett. 111 (17) (2017), 171603.
[11] D.F. Hanks, Z. Lu, J. Sircar, T.R. Salamon, D.S. Antao, K.R. Bagnall, E.N. Wang, Nanoporous membrane device for ultra high heat flux thermal management, Microsyst. Nanoeng. 4 (1) (2018) 1–10.
[12] D.F. Hanks, Z. Lu, J. Sircar, I. Kinefuchi, K.R. Bagnall, T.R. Salamon, E.N. Wang, High heat flux evaporation of low surface tension liquids from nanoporous membranes, ACS Appl. Mater. Interfaces 12 (6) (2020) 7232–7238.
[13] K.L. Wilke, B. Barabadi, T. Zhang, E.N. Wang, Controlled wetting in nanoporous membranes for thin film evaporation, J. Heat Transf. 138 (8) (2016).
[14] Y. Li, H. Chen, S. Xiao, M.A. Alibakhshi, C.W. Lo, M.C. Lu, C. Duan, Ultrafast diameter-dependent water evaporation from nanopores, ACS Nano 13 (3) (2019) 3363–3372.
[15] D.S. Antao, S. Adera, Y. Zhu, E. Farias, R. Raj, E.N. Wang, Dynamic evolution of the evaporating liquid–vapor interface in micropillar arrays, Langmuir 32 (2) (2016) 519–526.
[16] D.S. Antao, S. Adera, E. Farias, R. Raj, E.N. Wang, Visualization of the evaporating liquid-vapor interface in micropillar arrays, J. Heat Transf. 138 (2) (2016).
[17] Z. Lu, S. Narayanan, E.N. Wang, Modeling of evaporation from nanopores with nonequilibrium and nonlocal effects, Langmuir 31 (36) (2015) 9817–9824.

[18] D. Niu, G.H. Tang, The effect of surface wettability on water vapor condensation in nanoscale, Sci. Rep. 6 (1) (2016) 1–6.
[19] J. Fan, H. Wu, F. Wang, Evaporation-driven liquid flow through nanochannels, Phys. Fluids 32 (1) (2020), 012001.
[20] B. Ma, K. Guye, B. Dogruoz, D. Agonafer, Molecular dynamics simulations of thin-film evaporation: the influence of interfacial thermal resistance on a graphene-coated heated silicon substrate, Appl. Therm. Eng. 117142 (2021).
[21] X. Wang, Y. Li, J.A. Malen, A.J. McGaughey, Assessing the impact of disjoining pressure on thin-film evaporation with atomistic simulation and kinetic theory, Appl. Phys. Lett. 116 (21) (2020), 213701.
[22] Y. Akkus, A. Beskok, Molecular diffusion replaces capillary pumping in phase-change-driven nanopumps, Microfluid. Nanofluid. 23 (2) (2019) 1–9.
[23] Y. Akkus, A. Koklu, A. Beskok, Atomic scale interfacial transport at an extended evaporating meniscus, Langmuir 35 (13) (2019) 4491–4497.
[24] M. Ozsipahi, Y. Akkus, C.T. Nguyen, A. Beskok, Energy-based interface detection for phase change processes of monatomic fluids in nanoconfinements, J. Phys. Chem. Lett. 12 (34) (2021) 8397–8403.
[25] A.P. Thompson, H.M. Aktulga, R. Berger, D.S. Bolintineanu, W.M. Brown, P. S. Crozier, S.J. Plimpton, LAMMPS-a flexible simulation tool for particle-based materials modeling at the atomic, meso, and continuum scales, Comput. Phys. Commun. 271 (2022), 108171.
[26] M.S. Daw, S.M. Foiles, M.I. Baskes, The embedded-atom method: a review of theory and applications, Mater. Sci. Rep. 9 (7–8) (1993) 251–310.
[27] S. Maruyama, Y. Yamaguchi, A molecular dynamics simulation of a bubble nucleation on solid surface, in: Proceedings of the 5th ASME/JSME Joint Thermal Engineering Conference, March 15–19, San Diego, California, 1999.
[28] Y. Li, W. Zhou, Y. Zhang, B. Qi, J. Wei, A molecular dynamics study of surface wettability effects on heterogeneous bubble nucleation, Int. Commun. Heat Mass Transf. 119 (2020), 104991.